# Efficient method for computing the electronic transport properties of a multiterminal system

Leandro R. F. Lima, Amintor Dusko, and Caio Lewenkopf
*Instituto de Física, Universidade Federal Fluminense, 24210-346 Niterói, RJ, Brazil*

(Received 22 January 2018; published 4 April 2018)

We present a multiprobe recursive Green's function method to compute the transport properties of mesoscopic systems using the Landauer-Büttiker approach. By introducing an adaptive partition scheme, we map the multiprobe problem into the standard two-probe recursive Green's function method. We apply the method to compute the longitudinal and Hall resistances of a disordered graphene sample, a system of current interest. We show that the performance and accuracy of our method compares very well with other state-of-the-art schemes.

DOI: 10.1103/PhysRevB.97.165405

## I. INTRODUCTION

The recursive Green's function (RGF) method is a powerful tool to calculate the electronic transport properties of quantum coherent mesoscopic systems [1–4]. Several important improvements have been proposed over the last decades to improve the method performance, such as an optimal block-diagonalization scheme [5] and a modular RGF method [6,7], to name a few. Notwithstanding, with few exceptions so far the method has been mainly used to compute the Landauer conductance in two-terminal devices, that is, in systems attached to two leads in contact with electronic reservoirs.

Some studies [4,8–14] have extended the method to treat multiprobe systems. However, the latter are designed to address systems with very simple geometries, except for Ref. [10], at the expense of increasing the algorithm complexity.

In this paper, we report a multiprobe recursive Green's function (MPRGF) method that generalizes and improves the previous developments. Our scheme is simple to implement, very flexible, and capable of addressing systems with arbitrary geometry, and shows a superior or similar performance as compared to the others.

This paper is organized as follows: In Sec. II, we summarize the multiprobe Landauer-Büttiker approach and present expressions for the observables of interest cast in terms of Green's functions. In Sec. III, we introduce the adaptive partition scheme that allows for an efficient solution of the problem. We illustrate the method using a simple pedagogical model. Section IV shows an application of the MPRGF method in a physical system of current interest. The processing time and accuracy of the method are discussed in Sec. V. We summarize our results in Sec. VI.

## II. ELECTRONIC TRANSPORT PROPERTIES IN MULTIPROBE SYSTEMS

In this section, we present a brief summary of the main results of the Landauer-Büttiker approach to calculate the transport properties of a multiprobe quantum coherent mesoscopic system. The RGF method can be implemented for both a finite-element discretization of the Schrödinger equation [15,16] or a tight-binding model based on a linear combination of atomic orbitals [17,18]. For simplicity, in this paper, we consider nearest-neighbor tight-binding models that use a single orbital per site. The generalization to more realistic models is straightforward. With this restriction, we can use the same discrete notation for both above-mentioned Hamiltonian models.

In linear response theory, the multiterminal Landauer-Büttiker formula for the electronic current $I_\alpha$ at the terminal $\alpha$ reads [19–21] (see Fig. 1)

$$I_\alpha = \sum_{\beta=1}^{N} \mathcal{G}_{\alpha\beta}(V_\alpha - V_\beta), \tag{1}$$

where the greek letters label the terminals, $V_\alpha$ is the voltage applied to the $\alpha$ terminal, and $G_{\alpha\beta}$ is the conductance given by

$$\mathcal{G}_{\alpha\beta} = \frac{2e^2}{h}\int_{-\infty}^{\infty} dE\left(-\frac{\partial f}{\partial E}\right)T_{\alpha\beta}(E), \tag{2}$$

that is cast in terms of the the Fermi distribution $f(E) = [1 + e^{(E-\mu)/k_BT}]^{-1}$ and the transmission $T_{\alpha\beta}(E)$. The factor 2 assumes spin degeneracy. For cases where the system Hamiltonian depends explicitly on the electron spin projection, one incorporates this degree of freedom in the lattice basis, doubling its size.

The transmission $T_{\alpha\beta}(E)$ is given by [22]

$$T_{\alpha\beta}(E) = \mathrm{tr}[\mathbf{\Gamma}_\beta(E)\mathbf{G}^r(E)\mathbf{\Gamma}_\alpha(E)\mathbf{G}^a(E)], \tag{3}$$

where $\mathbf{G}^r = (\mathbf{G}^a)^\dagger$ is the retarded Green's function of the full system (central region and leads—see Fig. 1), whose computation is the central goal of this paper, while $\mathbf{\Gamma}_\alpha$ is the linewidth of the lead corresponding to the $\alpha$ terminal. Both $\mathbf{G}^r$ and $\mathbf{\Gamma}_\alpha$ are expressed in a discrete representation, where $\mathbf{G}^r$ has the dimension of the number of sites in the central region, and the dimension of $\mathbf{\Gamma}_\alpha$ is the number of sites at the $\alpha$-lead–central region interface. Following the standard prescription [16,17], the leads are considered as semi-infinite. The decay width is related to the embedding self-energy, namely,

$$\mathbf{\Sigma}^r_\alpha = \mathbf{V}^\dagger\mathbf{G}^r_\alpha\mathbf{V} \tag{4}$$

and

$$\mathbf{\Gamma}_\alpha = i[\mathbf{\Sigma}^r_\alpha - (\mathbf{\Sigma}^r_\alpha)^\dagger], \tag{5}$$

 

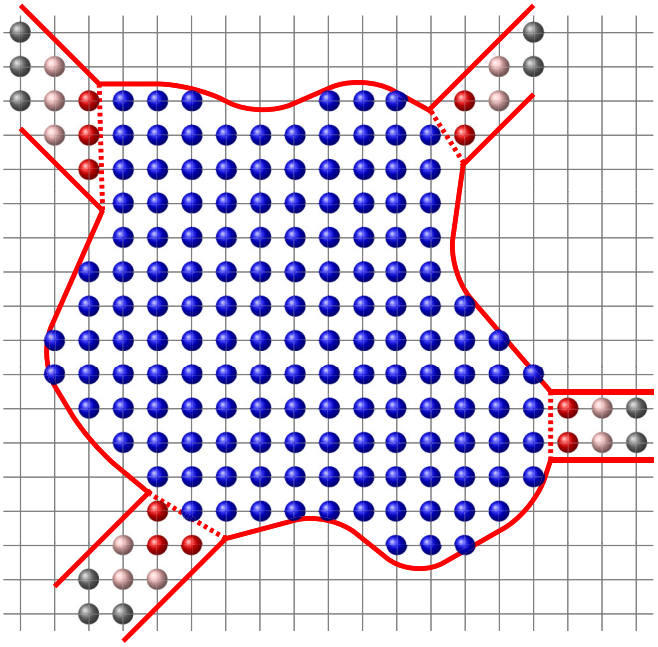

FIG. 1. Sketch of the mesoscopic system of interest. Blue sites compose the central region. The leads $\alpha = 1, \ldots, N_L$ are connected to electronic reservoirs in thermal and chemical equilibrium that act as terminals. The dashed lines indicate the lead–central region interfaces. Red, pink, and gray sites represent the first, second, and third primitive unit cells of different leads.

where $\mathbf{V}$ gives the coupling matrix elements between the lead $\alpha$ and the central region, and $\mathbf{G}^r_\alpha$ is a contact Green's function that casts the electron dynamics in the leads, which can be calculated in a number of ways [2,23–25].

The local density of states (LDOS) can be directly obtained from $\mathbf{G}^r$, namely,

$$\rho(j) = -\frac{1}{\pi}\mathrm{Im}\, G^r_{jj}, \tag{6}$$

where $j$ corresponds to the site at $\mathbf{r}_j$.

Another important quantity of interest is $T^\alpha_{jj'}$, the local transmission between two sites $j$ and $j'$ due to electrons injected from the terminal $\alpha$, namely [17,26],

$$T^\alpha_{jj'} = -2\,\mathrm{Im}\{[\mathbf{G}^r \mathbf{\Gamma}_\alpha \mathbf{G}^a]_{j,j'} H_{j',j}\}, \tag{7}$$

where $\mathbf{H}$ is the system Hamiltonian in the discrete representation.

## III. ADAPTIVE SLICING SCHEME

In this section, we put forward an efficient adaptive slicing scheme tailor-made for multiterminal systems. We present general expressions for the Green's functions and illustrate how the method works using a small and very simple lattice model, depicted in Fig. 2, which serves as a practical guide for the system labels we use. In what follows, we deal only with retarded Green's functions $\mathbf{G}^r$, where $E \to E + i\eta$. Hence, to simplify the notation, from now on we omit the superindex $r$.

The implementation of the RGF method requires a partition of the system into $N$ domains or "slices". A given slice $n$, that contains $M_n$ sites, is connected only with the slice $n-1$ and the slice $n+1$ through the hopping matrices $\mathbf{U}_{n,n-1}$ and $\mathbf{U}_{n,n+1}$, respectively, and has an internal hopping matrix $\mathbf{H}_n$. See the lattice model in Fig. 2 for details. Several partition schemes have been proposed in the literature [5,11,12]. As a rule, it is preferable to minimize the number of sites $M_n$ inside each slice $n$ and increase the number of slices $N$, since the computational time cost scales as $N \times M_n^3$.

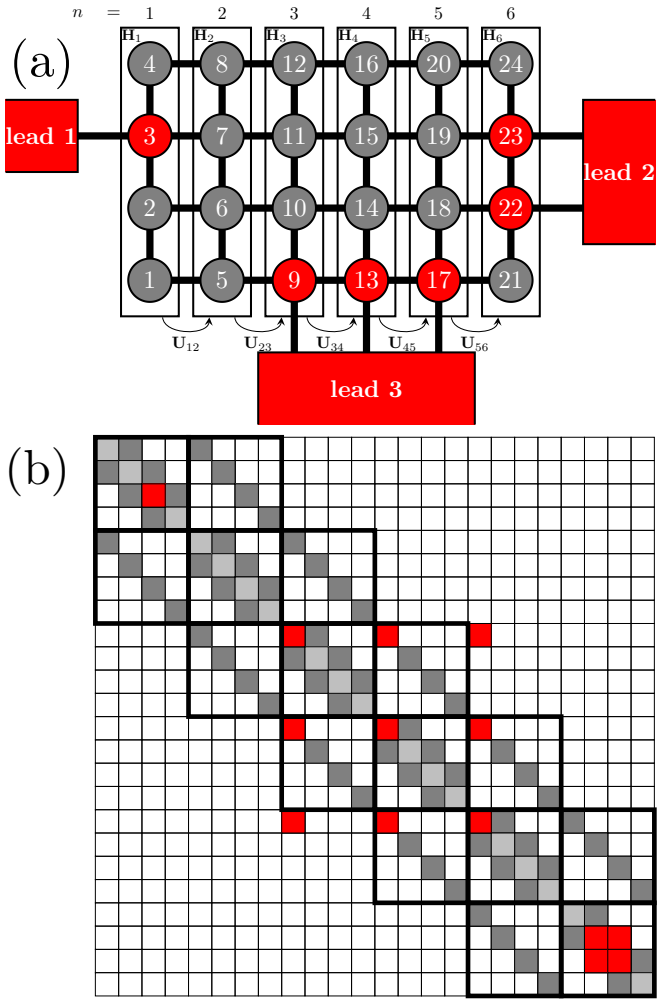


FIG. 2. (a) Standard RGF slicing scheme applied to a three-probe system with $N = 6$ slices with intraslice hopping matrices $\mathbf{H}_n$ and interslice hopping matrices $\mathbf{U}_{n,n+1}$ for $n = 1, \ldots, 6$. Each slice $n$ has $M_n = 4$ sites. (b) Matrix structure of $\mathbf{H} + \mathbf{\Sigma}$ for the system (a). White boxes correspond to $H_{ij} + \Sigma_{ij} = 0$ and the red ones to matrix elements where $\Sigma_{ij} \neq 0$. The thick solid lines highlight the intra- and interslice blocks.

For two-terminal geometries, it is convenient to connect the first $n = 1$ and the last $n = N$ slices to the left lead $L$ and to the right lead $R$, respectively. This partition scheme leads to a block tridiagonal Hamiltonian and a retarded self-energy $\mathbf{\Sigma}$ coupled only to the first and last slices of the system. Thus, in a block matrix representation, the self-energy has the form $\mathbf{\Sigma}_{n,n'} = \mathbf{\Sigma}_{1,1}\delta_{n,1}\delta_{n',1} + \mathbf{\Sigma}_{N,N}\delta_{n,N}\delta_{n',N}$, and $\mathbf{H} + \mathbf{\Sigma}$ has a block tridiagonal structure. As long as the last requirement is met, one can apply the RGF method straightforwardly.

Unfortunately, this simple scheme does not work for setups with more than two terminals. Figure 2 shows the standard RGF

slicing scheme applied to a very simple two-dimensional lattice system with three terminals. We show the lattice model in Fig. 2(a) and the corresponding matrix structure of $\mathbf{H}+\mathbf{\Sigma}$ for a nearest-neighbor coupling model Hamiltonian in Fig. 2(b). The matrix is sparse, as indicated by the white boxes (zero-value matrix elements). Here, $N=6$ and each slice $n=1,\ldots,6$ has $M_n=4$ sites. Note that the matrix elements due to terminal 3 spoil the tridiagonal block structure of $\mathbf{H}+\mathbf{\Sigma}$: Nonzero self-energy matrix elements appear in blocks other than the first and last slices (1 and 6) connecting simultaneously slices 3, 4, and 5. In more realistic cases of wider leads, the number of nonzero self-energy matrix elements increases and they appear further away from the tridiagonal block structure.

The RGF method has been modified over the years to account for multiple terminals. As mentioned in the Introduction, there are some well-established schemes for multiprobe RGF in use, such as the cross strip [4,8,9] and the circular [12] methods. All of them, including our scheme, are faster than the full inversion. Nevertheless, their efficiency depends strongly on the system symmetry. The partition scheme we present here finds an optimal set of slices with minimal $M_n$ for arbitrary system geometries and it is of very simple implementation.

Our MPRGF implementation relies on using the power and simplicity of the standard two-probe RGF equations [17] that is achieved by introducing an adaptive slicing scheme and a (single) virtual lead [5]. This is done in two main steps.

(i) *Adaptive partition*. We start the recursion with a virtual "left" lead composed by all the contact sites in the leads, which we call slice $n=0$. We define the slice $n=1$ by the sites that are connected to any lead $\alpha=1,\ldots,N_L$, where $N_L$ is the number of leads attached to the system. The next slices $n=2,3,\ldots$ are composed by the sites that are connected to sites that belong to the $n-1$ slice. This procedure is repeated $N$ times until all lattice sites are assigned to a slice. This scheme gives a block tridiagonal $\mathbf{H}$ (see mapping below) in an $N\times N$ block matrix representation. Figure 3(a) shows the proposed slicing scheme applied to the system of Fig. 2. We use different shapes and colors to indicate the slice each site belongs.

(ii) *Site label reassignment*. We renumber the sites in the system according to the lead they are attached and the slice they belong in increasing order as follows. The sites in $n=1$ are numbered in increasing order according to the leads to which they are connected. The number of sites connected to the lead $\alpha$ is $M_{1\alpha}$. Thus, the total number of sites in the $n=1$ slice is $M_1=\sum_{\alpha=1}^{N_L} M_{1\alpha}$. We divide the slice $n=1$ into $\alpha=1,\ldots,N_L$ sub-blocks, where the $\alpha$ block contains the $M_{1\alpha}$ sites connected to the lead $\alpha$ and has dimension $M_{1\alpha}\times M_{1\alpha}$. The self-energy matrix $\mathbf{\Sigma}$ has nonzero elements only in the sub-blocks $\mathbf{\Sigma}_{1,1}^{\alpha,\alpha}$ due to each real lead $\alpha$. The numbering of sites in the slices $n\geqslant 2$ can follow any specific order as long as each site in slice $n$ has a higher number than any site in slice $n-1$.

For clarity, let us explicitly implement this scheme for the model system of Fig. 2. Figure 3(a) shows the result. The sites connected to the leads that were originally numbered as 3, 9, 13, 17, 22, and 23 in Fig. 2(a) constitute the $n=1$, with $M_{11}=1$, $M_{12}=2$, and $M_{13}=3$ sites connected to leads 1, 2, and 3, respectively, that give $M_1=6$. Figure 3(a) indicates the sites in slice $n=1$ as red circles. We find this site label reassignment convenient, but is certainly not unique.

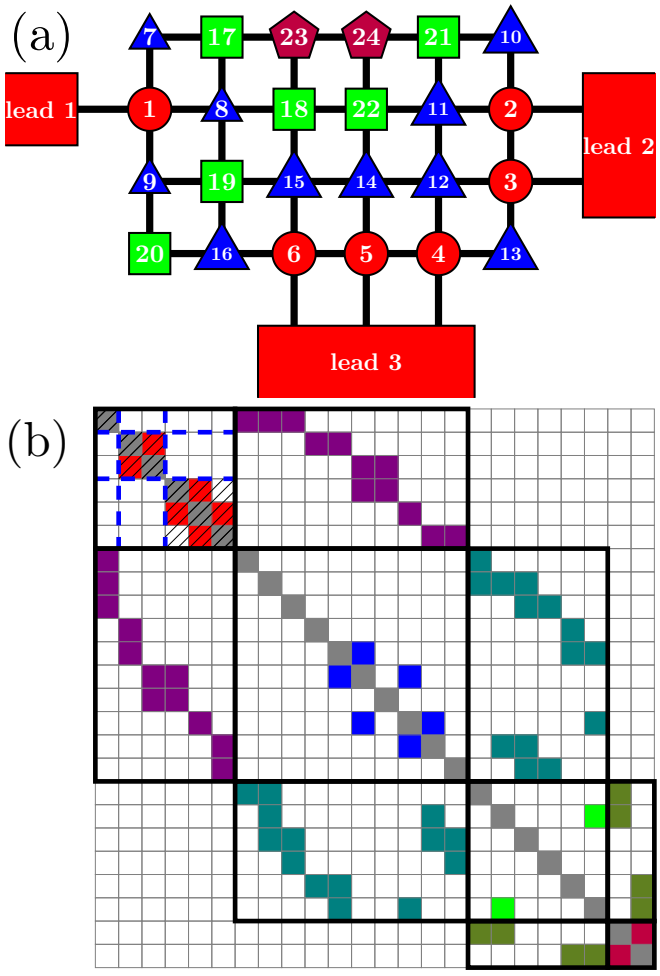


FIG. 3. MPRGF slicing scheme applied to the system in Fig. 2. (a) shows the sites with their new labels. Red circles, blue triangles, green squares, and purple pentagons represent sites belonging to the first, second, third, and fourth slices, respectively. (b) is the representations of the matrix $\mathbf{H}+\mathbf{\Sigma}$ corresponding to the slicing scheme in (a). The thick solid lines highlight the intra- and interslice blocks while the thick dashed lines correspond to the sub-block division of the slice 1 (see the main text for details). The hatched pattern represents the contribution from the self-energy $\mathbf{\Sigma}$ that acts only on the diagonal sub-blocks of slice 1 due to its ordering by leads.

Next, the sites connected to the $n=1$ are the sites with the original labels 2, 4, 5, 7, 10, 14, 18, 19, 21, and 24. These ten sites belonging to slice 2 are renumbered from 7 to 16 and shown in Fig. 3(a) as blue triangles. Following this protocol, $n=3$ has six sites (1, 6, 8, 11, 15, 20) renumbered from 17 to 22 and represented as green squares, while $n=4$ contains two sites (12, 16) renumbered as 23 and 24 being represented by purple pentagons in Fig. 3(a).

Figure 3(b) shows the corresponding matrix structure of $\mathbf{H}+\mathbf{\Sigma}$. Obviously the matrix has the same sparsity as before, but the size of the blocks can become larger than those expected in the standard RGF depending on the system. Each diagonal sub-block of the block $n=1$ is filled by the self-energy of one lead.

In this example we see that this slicing scheme is simple and fast to implement. It is possible to introduce optimizations to

the slicing scheme, such as the one developed for two probes in Ref. [5] based on the theory of graphs, at the cost of increasing the coding complexity. This discussion is beyond the scope of the present work.

Now we have all the ingredients to calculate the Green's functions using the RGF method. As standard, the free Green's functions are defined by setting the interslice hopping matrices $\mathbf{U}_{n,n+1} = 0$. By turning on the interslice matrices $\mathbf{U}_{n,n+1}$ we write a Dyson equation for the fully connected system. We perform left and right recursions using the equations [17]

$$\mathbf{G}^L_{n,n} = \left(\mathbf{E} - \mathbf{H}_n - \mathbf{U}_{n,n-1}\mathbf{G}^L_{n-1,n-1}\mathbf{U}_{n-1,n}\right)^{-1}, \quad (8)$$

$$\mathbf{G}^R_{n,n} = \left(\mathbf{E} - \mathbf{H}_n - \mathbf{U}_{n,n+1}\mathbf{G}^R_{n+1,n+1}\mathbf{U}_{n+1,n}\right)^{-1}, \quad (9)$$

where $\mathbf{G}^L_{n,n}$ ($\mathbf{G}^R_{n,n}$) is the Green's function of the slice $n = 1,\ldots,N$ when all the $k$ slices at its "left" with $k < n$ ("right" with $k > n$) are already connected. The recursions in Eqs. (8) and (9) start at $n = 1$ and $n = N$, respectively, and depend on the surface Green's functions of the virtual leads $\mathbf{G}^L_{0,0}$ and $\mathbf{G}^R_{N+1,N+1}$. The latter are obtained by standard procedures [17,23]. Since in our scheme all terminals are coupled to a single left virtual lead and the right virtual lead is uncoupled, we write

$$\mathbf{G}^L_{1,1} = (\mathbf{E} - \mathbf{H}_1 - \mathbf{\Sigma}_{1,1})^{-1}, \quad (10)$$

$$\mathbf{G}^R_{N,N} = (\mathbf{E} - \mathbf{H}_N)^{-1}, \quad (11)$$

where $\mathbf{\Sigma}_{1,1} \equiv \mathbf{U}_{1,0}\mathbf{G}^L_{0,0}\mathbf{U}_{0,1}$ is block diagonal because the real leads are decoupled, as we show in Fig. 3(b).

Figure 4 shows how the adaptive slicing scheme maps the lattice of Fig. 3(a) into an equivalent two-terminal system lattice with a virtual left lead containing all the real leads and an uncoupled virtual right lead.

The local Green's functions of the fully connected system $\mathbf{G}_{n,n}$ are given by [17]

$$\mathbf{G}_{n,n} = \left(\mathbf{E} - \mathbf{H}_n - \mathbf{U}_{n,n-1}\mathbf{G}^L_{n-1,n-1}\mathbf{U}_{n-1,n} - \mathbf{U}_{n,n+1}\mathbf{G}^R_{n+1,n+1}\mathbf{U}_{n+1,n}\right)^{-1}. \quad (12)$$

Using Eq. (12) we can directly calculate local properties such as the LDOS for all the sites in the system by simply extracting the diagonal elements of $\mathbf{G}_{n,n}$ for all $n$ and using Eq. (6).

To calculate the transmission matrix elements given by Eq. (3), we need the Green's functions components $\mathbf{G}_{1,1}$ connecting sites attached to different real leads. The Green's function $\mathbf{G}_{1,1}$ has dimension $M_1$ and reads

$$\mathbf{G}_{1,1} = \begin{pmatrix} \mathbf{G}^{1,1}_{1,1} & \mathbf{G}^{1,2}_{1,1} & \cdots & \mathbf{G}^{1,N_L}_{1,1} \\ \mathbf{G}^{2,1}_{1,1} & \mathbf{G}^{2,2}_{1,1} & \cdots & \mathbf{G}^{2,N_L}_{1,1} \\ \vdots & \vdots & & \vdots \\ \mathbf{G}^{N_L,1}_{1,1} & \mathbf{G}^{N_L,2}_{1,1} & \cdots & \mathbf{G}^{N_L,N_L}_{1,1} \end{pmatrix}, \quad (13)$$

where each sub-block $\mathbf{G}^{\alpha,\beta}_{1,1}$ of dimension $M_{1\alpha} \times M_{1\beta}$ represents the propagator between all the $M_{1\alpha}$ sites connected to the lead $\alpha$ and all the $M_{1\beta}$ sites connected to the lead $\beta$. Note that the sub-block division of the slice $n = 1$ for $\mathbf{H} + \mathbf{\Sigma}$ naturally renders to the sub-block division of $\mathbf{G}_{1,1}$ in Eq. (13) [see the example in Fig. 3(b)].

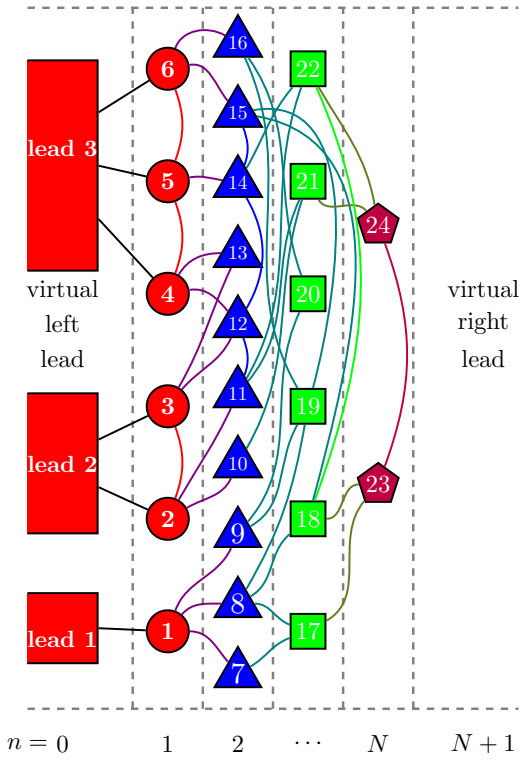


FIG. 4. Slicing scheme for the three-terminal model system. The site representation (colors and shapes) is the same as in Fig. 3(a). The dashed lines mark the slice divisions and the solid lines represent the bonds between sites. The left virtual leads contains all the real leads attached to the system and the right virtual lead is empty.

If we are interested only in the total transmissions, we need to perform only the right sweep in Eq. (9) for $n = N,\ldots,2$ and calculate $\mathbf{G}_{1,1}$ using Eq. (12) for $n = 1$. The calculation of other local properties such as the local transmissions $T^{\alpha}_{jj'}$ in Eq. (7) requires the Green's function components that connect the sites of interest $j$ and $j'$, that belong to slices $n$ and $n'$, respectively, and the sites attached to any lead $\alpha$, that belong to $n = 1$. Thus, we need the full Green's function blocks $\mathbf{G}_{n,1}$.

We calculate $\mathbf{G}_{n,1}$ by means of the extra recursions [17]

$$\mathbf{G}^L_{n,1} = \mathbf{G}^L_{n,n}\mathbf{U}_{n,n-1}\mathbf{G}^L_{n-1,1}, \quad (14)$$

$$\mathbf{G}_{n,1} = \mathbf{G}_{n,n}\mathbf{U}_{n,n-1}\mathbf{G}^L_{n-1,1}, \quad (15)$$

where, as before, $n = 2,\ldots,N$ and the label $L$ indicates that the Green's function $\mathbf{G}^L_{n,1}$ is the propagator between slices $n$ and 1 when all the slices between them are connected. Note that in distinction to the two-terminal RGF, here it is not necessary to compute $\mathbf{G}_{N,n}$, $\mathbf{G}_{n,N}$, and $\mathbf{G}_{1,n}$. Those matrices are not necessary because all the leads are connected only to the slice 1, as we show in Fig. 4.

Once again we use the sub-block representation to write

$$\mathbf{G}_{n,1} = \begin{pmatrix} \mathbf{G}^1_{n,1} \\ \mathbf{G}^2_{n,1} \\ \vdots \\ \mathbf{G}^{N_L}_{n,1} \end{pmatrix}, \quad (16)$$

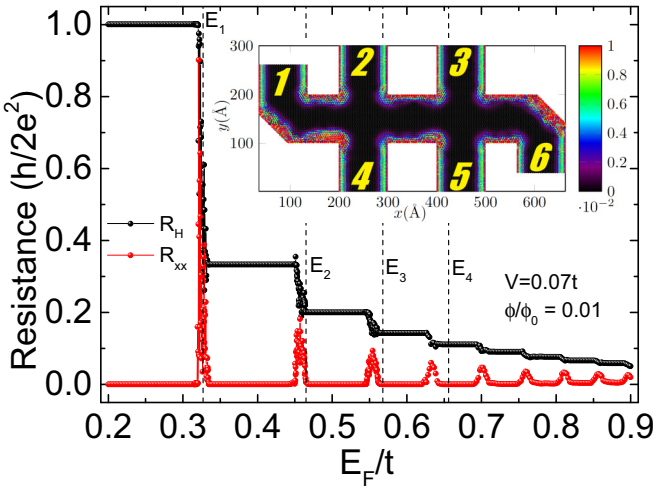


FIG. 5. Longitudinal $R_{xx}$ and Hall $R_H$ resistances as functions of the electronic energy $E_F$ for a constant magnetic flux $\phi/\phi_0 = 0.01$ and $V = 0.07t$. The dashed lines mark the analytical value of the Landau levels $E_n$ for $n = 1$, 2, 3, and 4 (see text for details). The inset shows the geometry used in the MPRGF calculations. Each arm and the main branch of the Hall bar are 100 Å wide. The color map shows the LDOS in arbitrary units for $E_F = 0.2t$ where one transport channel is open.

where each sub-block $\mathbf{G}^{\alpha}_{n,1}$ is the Green's function that connects all the $M_{1\alpha}$ sites contained in slice $n = 1$ that are attached to the lead $\alpha$ to all the $M_n$ sites in the slice $n$. For instance, by inspecting Fig. 4, one easily concludes that $\mathbf{G}^{3}_{2,1}$ is a $10\times3$ matrix connecting the sites $7,\ldots,16$ at slice 2 to the sites 4, 5, 6 in slice 1 that are attached to lead 3.

We stress that, for simplicity, we have only discussed lattice Hamiltonians with nearest-neighbor coupling terms. The method and equations presented here apply to any number of next-nearest neighbors, namely, second, third, and so on, which is of particular interest for tight-binding models based on maximally localized Wannier functions or related developments (see, for instance, Ref. [27]). Obviously, the inclusion of next-nearest neighbors increases $M_n$, since each slice $n$ is composed by all the sites connected to the $n-1$ partition, and decreases with the number of slices $N$. As a consequence, both the computational time and the memory usage increase with the reach of hopping integrals.

## IV. APPLICATION

Let us illustrate the power of the method by calculating longitudinal and Hall resistances for a disordered graphene monolayer sample submitted to a strong perpendicular magnetic field $B$ in a Hall-bar geometry with six terminals (see Fig. 5).

The electronic properties of the system are modeled by a nearest-neighbor tight-binding Hamiltonian with disordered on-site energy [28,29], namely,

$$H = -\sum_{\langle i,j\rangle} t_{i,j} c_i^{\dagger} c_j + \sum_j \epsilon_j c_j^{\dagger} c_j, \tag{17}$$

where the operator $c_j^{\dagger}$ ($c_j$) creates (annihilates) one electron at the $p_z$ orbital of the $j$th atom of the graphene honeycomb lattice. The first sum runs through nearest-neighbor atoms. The hopping matrix element between sites $i$ and $j$ is $t_{i,j} = te^{i\varphi_{ij}}$, where $t = 2.7$ eV is the hopping integral for graphene [28] and $\varphi_{ij}$ is the standard Peierls phase acquired in the path from $i$ to $j$ due to the presence of a magnetic field. The magnetic field is accounted for by a vector potential in the Landau gauge, namely, $\mathbf{A} = Bx\hat{\mathbf{y}}$. The corresponding Peierls phase reads [17]

$$\varphi_{ij} = \frac{e}{\hbar}\int_{\mathbf{r}_i}^{\mathbf{r}_j} \mathbf{A}\cdot d\mathbf{l} = 2\pi\frac{\phi}{\phi_0}\frac{(x_j + x_i)(y_j - y_i)}{a_0^2\sqrt{3}}, \tag{18}$$

where $\mathbf{r}_j = x_j\hat{\mathbf{x}} + y_j\hat{\mathbf{y}}$ is the site $j$ position, $a_0 = 2.46$ Å is the graphene lattice parameter, $\phi_0 = h/e$ is the magnetic flux quantum, and $\phi$ is the magnetic flux through one hexagon of the graphene lattice, namely, $\phi = BA_H$, where $A_H = a_0^2\sqrt{3}/2$. We use the Anderson model for the on-site disorder, where $\epsilon_j$ is randomly chosen from a uniform distribution in the interval $[-V, V]$. The disorder strength is taken as $V = 0.07t$ and the magnetic flux is $\phi/\phi_0 = 0.01$. The results presented below correspond to a single disorder realization.

Using the MPRGF technique described in Sec. III, we calculate the zero-temperature conductance matrix $\mathcal{G}_{\alpha\beta} = (2e^2/h)T_{\alpha\beta}$ given by Eq. (2). We avoid spurious mode mismatch at the lead-sample interface, without the need of changing the gauge [30], by using vertical leads in all six terminals of the Hall bar (see the inset of Fig. 5).

In linear response, the multiterminal Landauer-Büttiker formula [19–21], Eq. (1), gives the current $I_\alpha$ at terminal $\alpha$ as a function of the voltages $V_\beta$ at all terminals $\beta = 1,\ldots,6$. We set terminals $\alpha = 2$–5 as voltage probes with $I_2 = I_3 = I_4 = I_5 = 0$ to compute the current between terminals 1 and 6, namely, $I \equiv I_1 = -I_6$. See the inset of Fig. 5. We obtain the longitudinal and Hall resistances using $R_{xx} = |V_4 - V_5|/I$ and $R_H = |V_3 - V_5|/I$, respectively [15,20,21].

Figure 5 shows the resistances $R_{xx}$ and $R_H$ as functions of the electronic energy $E_F$. We have chosen $\phi/\phi_0$ such that the system is in the quantum Hall (QH) regime. The quantized nature of the QH effect is clearly manifest for energies where $R_{xx} = 0$ and $R_H = h/2e^2(2|n|+1)$, where $2|n|+1$ is the number of propagating channels (without spin) and $n$ is the Landau level (LL) index [15,21]. The position of the first peak in Fig. 5 matches the analytical value $E_1 = \sqrt{3/2}ta_0/\ell_B$ calculated using the Dirac Hamiltonian, that effectively describes the low-energy dynamics of electrons in graphene $|E_F| \ll t$ [28,31]. When $E_F$ matches $E_n$, the energy of the Landau level $n$, backscattering becomes available through the LL flatband channel yielding a peak in $R_{xx}$. As expected, as one increases $|E_F|/t$, the Dirac Hamiltonian is no longer a good approximation and the numerically obtained values of the LL energies increasingly deviate from the analytical prediction $E_n = E_1\sqrt{n}$ [32].

The MPRGF method is also employed to calculate the LDOS, Eq. (6). The system geometry (see the inset of Fig. 5) has armchair and zigzag edges along the vertical and horizontal directions [32], respectively, and a rough tilted edge with no high symmetry crystallographic orientation near terminals 1 and 6. The inset shows that the LDOS is roughly constant along the zigzag edges. A similar behavior is not observed neither

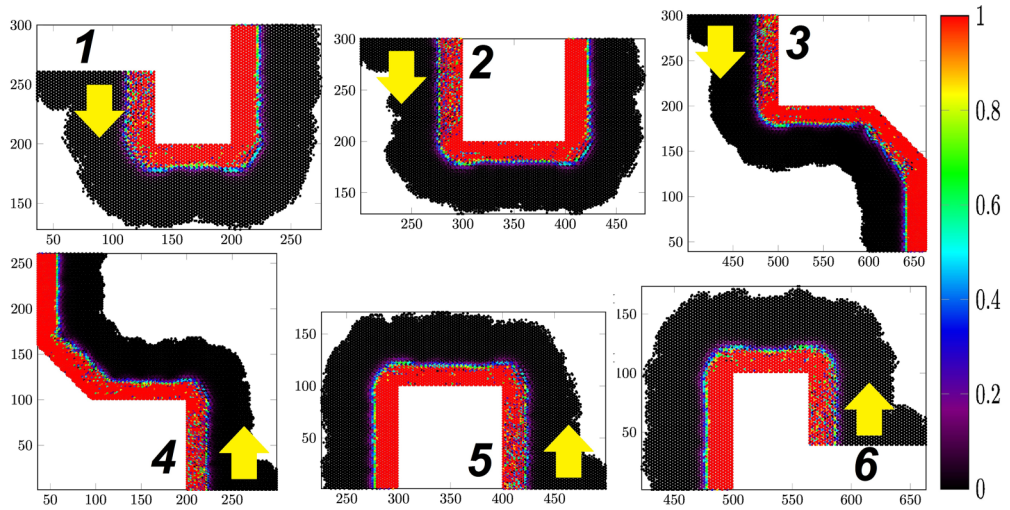


FIG. 6. Local transmission in arbitrary units for $E_F = 0.2t$. The panels consider settings where the electrons are injected from different terminals, indicated by the corresponding labels and arrows. We show only nonvanishing transmissions. The parameters are the same as in Fig. 5.

in armchair nor in chiral edges. This indicates that in the QH regime the electron propagation along zigzag edges is more robust against bulk and edge disorder than the propagation along edges with other crystallographic directions, reminiscent of the behavior observed in the absence of an external magnetic field [33].

Figure 6 shows the local transmission calculated according to Eq. (7). Here, we set $E_F = 0.2t$, corresponding to the first Hall plateau. We find that the enhanced LDOS at opposite edges of the Hall bar observed in the inset of Fig. 5 corresponds indeed to transmissions in opposite directions. Electrons injected from one terminal propagate along the system edges to the next terminal on the "left" due to the strong magnetic field. The edge current profile depends very weakly on which terminal the electrons are injected or on the edge crystallographic orientation, which is in contrast to the LDOS behavior in Fig. 5 (inset).

## V. BENCHMARK

Let us now analyze the performance and accuracy of the MPRGF method. We compare the computational time required to calculate the transmission matrix in a six-terminal Hall bar as depicted in Fig. 7 by means of direct diagonalization, circular slicing [12], and the proposed adaptive scheme.

The circular scheme, depicted in Fig. 7(a), leads to a number $M_n$ of sites inside a slice $n$ that depends linearly on $L$ and $W$ simultaneously. Since the number of operations in the standard RGF scheme depends on the weight $w = \sum_{n=1}^{N} M_n^3$, the typical runtime of a circular slicing algorithm scales as $w \propto (LW^3 + WL^3)$. Thus, the computational time scales cubically with the largest of $L$ and $W$. On the other hand, in the MPRGF, the number of sites inside each cell depends mainly on $W$ while the number of slices $N$ depends mainly on $L$, which results in a computational time that scales with $LW^3$. In both cases, the CPU time scales approximately as $L^4$ if the system has aspect ratio $W/L \approx 1$.

Figure 8 shows the computational time to calculate the full transmission matrix for the system in Fig. 7 as a function of the length $L$, where $L \gg W$. Here, we consider a two-dimensional electron gas (2DEG) described by a discretized Hamiltonian in a square-lattice representation with nearest-neighbor hopping matrix elements. Using the finite-difference method [15,16], the discretization of the Schrödinger Hamiltonian in two dimensions leads to a "hopping" parameter $-t$, where $t = \hbar^2/(2m^*a^2)$, $m^*$ is the electron effective mass, and $a$ is the grid spacing in both $x$ and $y$ directions. We calculate the

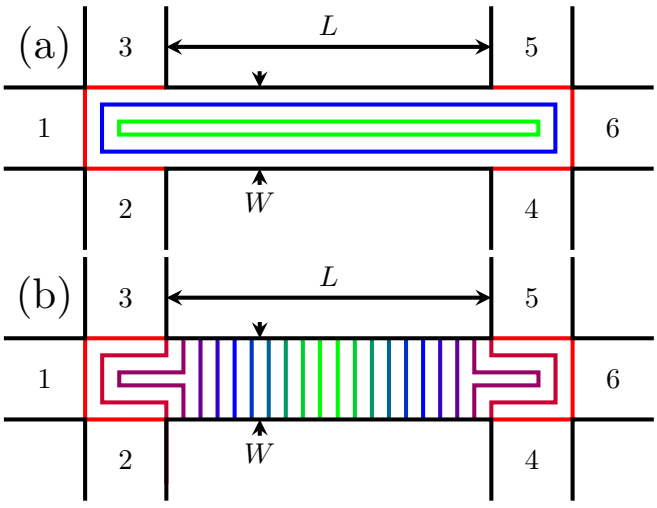


FIG. 7. Schematic comparison between the slicing scheme used in the circular slicing and the MPRGF that we propose applied to a Hall-bar geometry. (a) The circular slicing provides slices that contain sites along both longitudinal and transverse directions, corresponding to dimensions $L$ and $W$. The first slice of this recursive method is the largest one, containing all the sites that are connected to the leads plus extra sites along the length $L$. The slice sizes decrease towards the center of the system as the last slice is the smallest one. (b) The MPRGF slicing scheme ensures that the first slice contains all the sites connected to the leads, rendering a smaller number of sites inside the first slice and a larger number of slices.

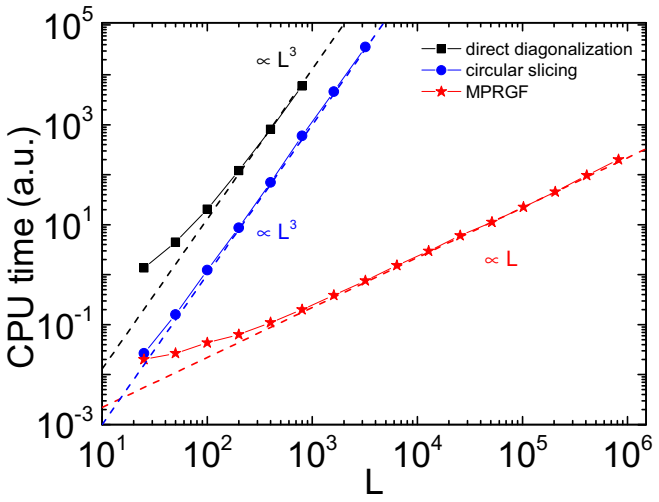


FIG. 8. Computational time in arbitrary units (single processor) to calculate the full transmission matrix of the system depicted in Fig. 7 as a function of $L$ for $W = 10$ using direct diagonalization (black squares), circular slicing (blue circles), and the proposed MPRGF (red stars).

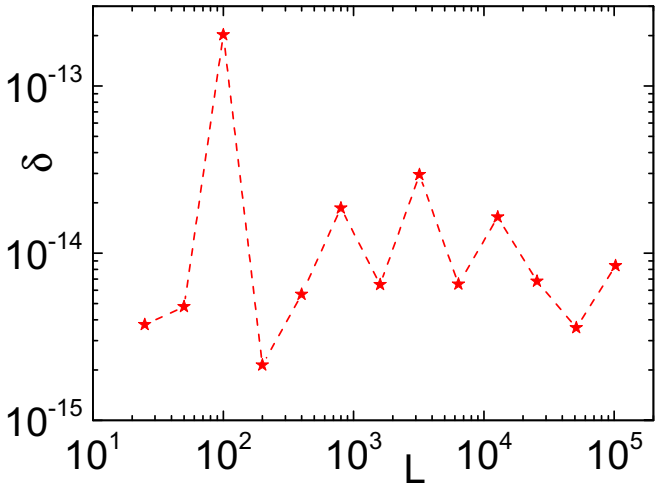


FIG. 9. Accuracy estimate $\delta$ for the numerical calculation of the system Green's functions as a function of the system length $L$ for $W = 10$. See the main text for details.

transmission for the electron energy $E_F = 0.01t$ for systems with $W = 10$ sites.

We find that, for large $L$, the runtime of the adaptive scheme indeed scales linearly with $L$ while both direct diagonalization and the circular slicing scale as $L^3$ as discussed. The power-law dependences, which are intrinsic to the methods, render a performance to the proposed MPRGF that is orders of magnitude better than the other codes for $L \gg W$.

Hybrid slicing schemes have been proposed to optimize the RGF method for particular system geometries. Some examples are the cross strip [4,8,9] and the mixed circular [12] schemes. In these works the partition of the system region connected to the leads is designed based on the specificities of the sample geometry, while the rest of the system is sliced by the standard method. Another nice multiprobe approach is the "knitting" one [10], that does not require a partition scheme. These procedures show a good computational performance, but the coding complexity is increased. We stress that our scheme does not rely on specific features of the sample (or leads) geometry, since it extracts from the Hamiltonian all the information needed for determining the optimal partitions.

Let us now discuss the accuracy of the adaptive scheme. It is possible to quantify the precision of the method by comparing $(\mathbf{E} - \mathbf{H} - \mathbf{\Sigma})\mathbf{G}$ with the unit matrix $\mathbf{1}$. This straightforward scheme cannot be used since the recursive method avoids the calculation of a large number of full Green's function matrix elements. However, since $\mathbf{G}_{n,n}$ and $\mathbf{G}_{n,1}$ are available, we can estimate the precision by evaluating $\delta \equiv \text{maxval}[|\sum_n (\mathbf{E} - \mathbf{H} - \mathbf{\Sigma})_{1,n}\mathbf{G}_{n,1} - \mathbf{1}|]$, where maxval returns the maximum value of the elements in the matrix. Figure 9 shows the deviation $\delta$ as a function of the length $L$ for the system depicted in Fig. 7. By computing $\mathbf{G}$ in double precision, we find that $\delta$ does not systematically increase with $L$, supporting the confidence on the algorithm stability, and it remains roughly within $10^{-14} \cdots 10^{-13}$, which is four orders of magnitude smaller than the deviations reported using similar methods [11].

We conclude this section by discussing the effect of the regularization parameter $\eta$ in the calculations. In our approach, $\eta$ is only necessary for the computation of the contact Green's function [23] and is introduced only in the first decimation loop to guarantee fast convergence. We find that this procedure leads to a contact Green's function $\mathbf{G}_\alpha$ that does not depend on the choice of $\eta$ and minimizes the deviation between the calculated numerical value of $\mathbf{G}_\alpha$ and the one obtained by analytical expressions for one-dimensional (1D) chains. Since we use the $\Sigma^r$ extracted from the contact Green's functions, in general it is not necessary to introduce $\eta$ for the computation of the central region Green's functions. The "$\eta$-free" calculation of the system Green's function renders the numerical precision reported in this paper.

## VI. SUMMARY

In this paper, we have put forward a multiprobe recursive Green's function method to compute the transport properties of a quantum phase-coherent system using the Landauer-Büttiker approach.

By applying the adaptive slicing scheme put forward in Sec. III, we write the $\mathbf{H} + \mathbf{\Sigma}$ matrix in block tridiagonal form. In this representation, all leads belong to a "left" virtual lead. Hence, the central region sites connected to the leads belong to the $n = 1$ slice and there is no "right" virtual lead attached to the slice with the largest partition slice $n = N$. This mapping allows one to use the standard RGF equations, designed to compute only the full Green's function matrix elements necessary to calculate the transport quantities of interest, such as LDOS, local, and total transmissions.

The slicing scheme we put forward allows one to address multiterminal systems with arbitrary geometries and multiorbital tight-binding Hamiltonians with hopping terms that include more than nearest neighbors (at the expense of increasing CPU time). Our method is exact, since the Green's

functions are calculated using the standard RGF equations, which provide a fast and robust computational scheme that has been optimized and extensively tested over the years. Further, it allows for the inclusion of an electronic interaction via a mean-field approach where one needs to integrate the Green's functions in the complex plane weighted by the Fermi-Dirac distribution [34–37].

**ACKNOWLEDGMENTS**

We thank Dr. M. O. Goerbig for useful discussions. The authors acknowledge the financial support of the Brazilian funding agencies CNPq (Grants No. 308801/2015-6 and No. 400573/2017-2) and FAPERJ (Grants No. E-26/202.917/2015 and No. E-26/202.769/2016).

[1] D. J. Thouless and S. Kirkpatrick, J. Phys. C: Solid State Phys. **14**, 235 (1981).
[2] A. MacKinnon, Z. Phys. B **59**, 385 (1985).
[3] F. Sols, M. Macucci, U. Ravaioli, and K. Hess, J. Appl. Phys. **66**, 3892 (1989).
[4] H. U. Baranger, D. P. DiVincenzo, R. A. Jalabert, and A. D. Stone, Phys. Rev. B **44**, 10637 (1991).
[5] M. Wimmer and K. Richter, J. Comput. Phys. **228**, 8548 (2009).
[6] S. Rotter, J.-Z. Tang, L. Wirtz, J. Trost, and J. Burgdörfer, Phys. Rev. B **62**, 1950 (2000).
[7] F. Libisch, S. Rotter, and J. Burgdörfer, New J. Phys. **14**, 123006 (2012).
[8] H. U. Baranger, A. D. Stone, and D. P. DiVincenzo, Phys. Rev. B **37**, 6521 (1988).
[9] H. U. Baranger, Phys. Rev. B **42**, 11479 (1990).
[10] K. Kazymyrenko and X. Waintal, Phys. Rev. B **77**, 115119 (2008).
[11] Y. Mou, R. Xian-Jin, C. Yan, and W. Rui-Qiang, Chin. Phys. B **20**, 097201 (2011).
[12] G. Thorgilsson, G. Viktorsson, and S. Erlingsson, J. Comput. Phys. **261**, 256 (2014).
[13] Z. Qi, D. A. Bahamon, V. M. Pereira, H. S. Park, D. K. Campbell, and A. H. Castro Neto, Nano Letters. **13**, 2692 (2013).
[14] V. Torres, D. Faria, and A. Latgé, arXiv:1802.09415 (2018).
[15] S. Datta, *Electronic Transport in Mesoscopic Systems* (Cambridge University Press, Cambridge, UK, 1995).
[16] D. K. Ferry, S. M. Goodnick, and J. Bird, *Transport in Nanostructures* (Cambridge University Press, Cambridge, UK, 2009).
[17] C. H. Lewenkopf and E. R. Mucciolo, J. Comput. Electron. **12**, 203 (2013).
[18] E. Ridolfi, L. R. F. Lima, E. R. Mucciolo, and C. H. Lewenkopf, Phys. Rev. B **95**, 035430 (2017).
[19] M. Büttiker, Y. Imry, R. Landauer, and S. Pinhas, Phys. Rev. B **31**, 6207 (1985).
[20] M. Büttiker, Phys. Rev. Lett. **57**, 1761 (1986).
[21] T. Ihn, *Semiconductor Nanostructures* (Oxford University Press, Oxford, UK, 2010).
[22] Y. Meir and N. S. Wingreen, Phys. Rev. Lett. **68**, 2512 (1992).
[23] M. P. Lopez Sancho, J. M. Lopez Sancho, and J. Rubio, J. Phys. F: Met. Phys. **15**, 851 (1985).
[24] A. R. Rocha, V. M. García-Suárez, S. Bailey, C. Lambert, J. Ferrer, and S. Sanvito, Phys. Rev. B **73**, 085414 (2006).
[25] M. Wimmer, Quantum Transport in Nanostructures: From Computational Concepts to Spintronics in Graphene and Magnetic Tunnel Junctions, Ph.D. thesis, University Regensburg, 2009 .
[26] A. Cresti, R. Farchioni, G. Grosso, and G. P. Parravicini, Phys. Rev. B **68**, 075306 (2003).
[27] P. D'Amico, L. Agapito, A. Catellani, A. Ruini, S. Curtarolo, M. Fornari, M. B. Nardelli, and A. Calzolari, Phys. Rev. B **94**, 165166 (2016).
[28] A. H. Castro Neto, F. Guinea, N. M. R. Peres, K. S. Novoselov, and A. K. Geim, Rev. Mod. Phys. **81**, 109 (2009).
[29] E. R. Mucciolo and C. H. Lewenkopf, J. Phys.: Condens. Matter **22**, 273201 (2010).
[30] O. Shevtsov, P. Carmier, C. Petitjean, C. Groth, D. Carpentier, and X. Waintal, Phys. Rev. X **2**, 031004 (2012).
[31] M. O. Goerbig, Rev. Mod. Phys. **83**, 1193 (2011).
[32] L. Brey and H. A. Fertig, Phys. Rev. B **73**, 195408 (2006).
[33] E. R. Mucciolo, A. H. Castro Neto, and C. H. Lewenkopf, Phys. Rev. B **79**, 075407 (2009).
[34] L. R. F. Lima and C. H. Lewenkopf, Phys. Rev. B **93**, 045404 (2016).
[35] T. Ozaki, Phys. Rev. B **75**, 035123 (2007).
[36] A. Croy and U. Saalmann, Phys. Rev. B **80**, 073102 (2009).
[37] D. A. Areshkin and B. K. Nikolić, Phys. Rev. B **81**, 155450 (2010).